

A numerical model of pin thread effect on material flow and heat generation in shear layer during friction stir welding

Z. Sun, C.S. Wu*

MOE Key Lab for Liquid-Solid Structure Evolution and Materials Processing, Institute of Materials Joining, Shandong University, Jinan, 250061 China



ARTICLE INFO

Keywords:
Friction stir welding
Threaded pin
Numerical analysis
Material flow
Heat generation
Temperature field

ABSTRACT

A novel method is proposed to analyze the effect of pin thread on the heat generation, temperature distribution and material flow field in friction stir welding (FSW). Based on the analysis of the interaction force between the thread groove and the workpiece material, special equations are derived to describe the effect of pin thread parameters on the material flow velocity inside thread grooves. These equations are combined with a three-dimensional transient CFD model to quantitatively analyze the effect of threaded pin profile on heat transfer and material flow in FSW. The results show that the average flow velocity and the downward z-component of material flow velocity near the pin side surface for threaded pin is higher than that for unthreaded pin. For a threaded pin, heat generation near pin side is a little bit increased, the area of TMAZ (thermo-mechanically affected zone) is broadened, especially the width of TMAZ near the bottom surface of the workpiece, and the pin thread can effectively improve the material flow near the pin tip. The calculated and measured thermal cycles and TMAZ boundary match with each other. Compared with the sliding mesh method, this model is easier to ensure the numerical robustness and save computational time.

1. Introduction

Friction stir welding (FSW) has been successfully used in joining various kinds of metals and alloys [1–3]. Tool geometry is the most influential aspect of the FSW process development [4]. The primary functions of the tool include the localized heating and material flow so that it plays a critical role in affecting the microstructures and mechanical properties of the weld joints [5–7]. A FSW tool typically consists of a rotating round shoulder and a threaded cylindrical pin, which generates heat locally by friction and drives the softened material to flow in the shear layer [8]. Features of the tool such as thread and flat on the pin surface are believed to improve material flow around the tool, promote oxide breakdown, increase the area of nugget zone, produce high quality welds and affect forces on tool [4,9–14].

It is reported that for clockwise rotation, a left-hand thread could push the material downward adjacent to the pin. Besides, it also led to driving an upward motion of material of an equivalent amount far away from the pin surface in the shear layer, and enhance material mixing in the weld vicinity [11,14]. It has been experimentally proven that during FSW, the threaded pin profile can avoid several defects which are likely to occur for an unthreaded pin [6,15,16]. Zhao et al. [6] used four different pins (column threaded pin, taper threaded pin, column pin and taper pin) to make comparison, and concluded that taper pin

with thread profile produced the best weld quality compared to others in terms of defect reduction and enhanced grain refinement. It is reported that wormhole defects are minimized or disappeared in weld nugget zone when threaded pin profile is used in place of unthreaded one for FSW [15,16]. The threaded pin promotes the material flow in a downward direction, thereby enhancing material transportation across the weld root. Ouyang et al. [17] found the presence of vortex-like structure formed by concentric flow lines for welding similar alloy and alternative lamellae of alloy components for welding dissimilar alloys, attributing to 'stir action' of a threaded pin. Therefore, a careful consideration of thread profile is vital for FSW tool design. However, for the thread design on pin side, there is a lack of scientific basis in practical application of engineering. Currently, the thread is designed empirically by trial and error. In addition, the underlying mechanism, in context to the variation of flow/thermal behavior with respect to threaded pin, is not properly documented.

In order to obtain dynamic information during FSW process, researchers attempted to observe the real-time plastic material flow around the threaded pin with the aid of sophisticated techniques such as computer tomography (CT) and tracer particles, etc. Schmidt et al. [18] investigated the material flow around the threaded tool by traditional metallography as well as X-ray and CT, and proposed the presence of different flow zones or layers across vicinity of the weldment.

* Corresponding author.

E-mail address: wucs@sdu.edu.cn (C.S. Wu).

Morisada et al. [19,20] visualized the material flow around the pin by real-time X-ray radiography using a tiny spherical tungsten tracer, and obtained the three-dimensional material flow path by following the locus of the tracer. They found a comparatively higher material flow velocity at retreating side (RS) compared to advancing side (AS).

Even though great efforts have been made to observe and characterize the difference of heat generation, temperature profile, material flow and joint quality for unthreaded and threaded pins, most of the experiment-based methods just give some qualitative information. A quantitative analysis of pin thread effects on heat generation and material flow behavior during FSW process is essential to interpret the mechanisms involved. Numerical simulation has been widely used in analyzing the thermo-mechanical process and material flow behavior in FSW to explore the physical nature of the process or to guide tool design [21–25]. Generally, researchers employ computational fluid dynamics (CFD) [21–23] and computational solid mechanics (CSM) [24,25] to model FSW process. Due to the advantages in numerical simulation of material flow, the CFD method has been more widely used in modeling FSW process with complex pin shapes [26–29]. In CFD models of FSW, velocity-based boundary condition [22,23] and shear stress-based boundary condition [30,31] are two categories to treat the contact condition at tool-workpiece interface.

In numerical simulation of the thermo-mechanical behavior and material flow in FSW process, some researchers did not take into consideration the thread features because the presence of threads brings the complexity and difficulty of modeling [32–35]. Other investigators indirectly considered the thread feature by simply applying a uniform vertical velocity at pin side [22,36–38]. Such a presetting of vertical material movement may oversimplify the pin thread effect.

On the other hand, some researchers directly dealt with the thread feature in the geometric model of the calculation domain, and applied special boundary conditions at the tool-workpiece interface [31,39–41]. When the contact conditions at tool-workpiece interface were supposed to be full sticking, no obvious movement of material along the vertical direction due to the presence of thread is predicted [39,40]. Atharifar et al. [41] set the contact condition as partial sticking/sliding. Chen et al. established a CFD model of FSW process by considering an alternative frictional boundary condition [31], and took into account the pin thread features by adopting sliding mesh method in their model [42]. The thread feature was treated as an extra fluid volume which rotates with the same speed as that of the tool and is geometrically connected to the surrounding fluid domain by the mesh interface. The simulation results shown that the interfacial sticking is preferable at the inside of the thread groove, and pin thread causes a many-circle flow pattern around the threaded pin. However, the effect of pin thread on the in-process phenomena during FSW has not been completely understood, and there is still a lack of theoretical guidance in thread design and tool manufacture.

In this study, a new method is proposed to consider the pin thread effects on materials flow and heat generation in FSW. Based on the analysis of the interaction force between the thread groove and the workpiece material, special equations are derived to describe the effect of pin thread parameters on the material flow velocity inside thread grooves, which are taken as the boundary conditions for material flow velocity. Then, a three-dimensional transient CFD model is developed to quantitatively analyze the effect of threaded pin profile on the heat generation, temperature field and material flow characteristics in FSW. Finally, the numerical simulation results are verified by experimentally measuring the thermal cycles and the TMAZ boundary.

2. Mathematical modeling

2.1. Governing equations

Fig. 1 shows a schematic illustration of FSW process and its geometrical model features for numerical simulation. The origin of the

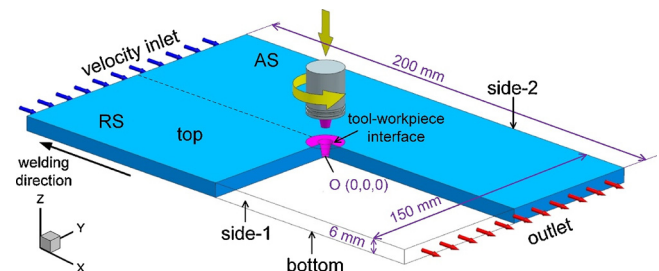


Fig. 1. A schematic of FSW process and its corresponding geometrical model.

Cartesian coordinate system is taken at the intersection point between the tool axis and bottom surface of the workpiece. The workpiece material is assumed as an incompressible single-phase non-Newtonian fluid. In order to simplify the FSW model, effects of tool shoulder concavity and tool tilt angle are ignored. The continuity, momentum and energy conservation equations are used to describe the heat transfer and material flow in FSW process.

The continuity equation,

$$\frac{\partial \rho}{\partial t} + \nabla \cdot (\rho \vec{v}) = 0 \quad (1)$$

The momentum equations,

$$\frac{\partial \rho \vec{v}}{\partial t} + \nabla \cdot (\rho \vec{v} \vec{v}) = -\nabla p + \nabla \cdot [\mu (\nabla \vec{v} + \nabla \vec{v}^T)] \quad (2)$$

The energy equation,

$$\rho c_p \frac{\partial T}{\partial t} + \rho c_p \nabla \cdot (\vec{v} \cdot T) = \nabla \cdot (k \nabla T) + S_v \quad (3)$$

where ρ is the density of material, c_p is the specific heat, \vec{v} is the velocity vector of the plastic material flow, t is the time, p is the pressure, μ is the material viscosity which is temperature and strain rate-dependent, k is the thermal conductivity, T is the temperature, and S_v is the viscous dissipation source due to plastic deformation in the shear layer, which can be expressed as [33,43],

$$S_v = \eta_v \mu \dot{\epsilon}^2 \quad (4)$$

where η_v represents the fraction of the viscous dissipation that is converted to heat, while $\dot{\epsilon}$ is the effective strain rate, which is calculated as follows,

$$\dot{\epsilon} = \sqrt{\frac{2}{3} \left(\left(\frac{\partial u_1}{\partial x_1} \right)^2 + \frac{1}{2} \left(\frac{\partial u_1}{\partial x_2} + \frac{\partial u_2}{\partial x_1} \right)^2 + \frac{1}{2} \left(\frac{\partial u_1}{\partial x_3} + \frac{\partial u_3}{\partial x_1} \right)^2 + \frac{1}{2} \left(\frac{\partial u_2}{\partial x_2} + \frac{\partial u_3}{\partial x_2} \right)^2 + \frac{1}{2} \left(\frac{\partial u_2}{\partial x_3} + \frac{\partial u_3}{\partial x_3} \right)^2 \right)} \quad (5)$$

where u_i is the velocity component, and x_i is the coordinate-axis directions.

2.2. Material properties

The density of AA6061 material is taken as constant, equals to 2700 kg/m³, while thermal conductivity and specific heat (c_p) are considered as temperature-dependent properties [43], which are given as below,

$$c_p = 929 - 6.27 \times 10^{-1} \times T + 1.48 \times 10^{-3} \times T^2 - 4.33 \times 10^{-8} \times T^3 \quad (6)$$

$$k = 25.2 + 3.98 \times 10^{-1} \times T + 7.36 \times 10^{-6} \times T^2 - 2.52 \times 10^{-7} \times T^3 \quad (7)$$

The fluid viscosity can be derived in terms of flow stress and effective strain rate [22,39,44],

$$\mu = \frac{\sigma_f}{3\dot{\epsilon}} \quad (8)$$

where the flow stress σ_f can be obtained based on the modified Sheppard-Wright constitutive equation [45,46],

$$\sigma_f = \frac{1}{\alpha} \ln \left\{ \left(\frac{Z}{A} \right)^{1/n} + \left[1 + \left(\frac{Z}{A} \right)^{2/n} \right]^{1/n} \right\} \cdot \frac{1}{2} \cdot \left\{ -\tanh \left(\frac{T - 750}{100} \right) + 1 \right\} \quad (9)$$

where α, A, n are constants related to the material properties, T is the temperature of the material, Z is Zener-Hollomon parameter, which is the temperature compensated strain rate, and can be written as,

$$Z = \dot{\epsilon} \exp \left(\frac{Q}{RT} \right) \quad (10)$$

where Q is the activation energy, R is the gas constant, and $\dot{\epsilon}$ is the effective strain rate which can be expressed as,

$$\dot{\epsilon} = \left(\frac{2}{3} \varepsilon_{ij} \varepsilon_{ij} \right)^{1/2} \quad (11)$$

where ε_{ij} is the strain rate tensor, defined as,

$$\varepsilon_{ij} = \frac{1}{2} \left(\frac{\partial u_i}{\partial x_j} + \frac{\partial u_j}{\partial x_i} \right)^{1/2} \quad (12)$$

where u is the velocity of the material, i, j represent x and y directions respectively.

2.3. Thermal boundary conditions

The boundary condition for heat exchange involves both convective and radiative heat transfer at the workpiece top surface away from tool shoulder edge. The heat flux boundary condition can be expressed as,

$$-k \frac{\partial T}{\partial z} = \sigma_r \varepsilon_r (T^4 - T_\infty^4) + h_t (T - T_\infty) \quad (13)$$

where σ_r is the Stefan-Boltzmann constant, ε_r is the external emissivity, h_t is the convective heat transfer coefficient at the top surface of the workpiece, and T_∞ is the ambient temperature. In this study, $\sigma_r = 5.67 \times 10^{-8} \text{ W}/(\text{m}^2 \text{ K}^4)$, $\varepsilon_r = 0.2$ [47], $h_t = 30.0 \text{ W}/(\text{m}^2 \text{ K})$ [48], $T_\infty = 300 \text{ K}$.

At the side and bottom surfaces of the workpiece, due to intimate contact of the workpiece with the backing plate and clamping equipment which are made of #45 steel, the boundary condition for heat exchange involves equivalent convective heat transfer. The heat flux boundary condition can be expressed as,

$$-k \frac{\partial T}{\partial n} = h_b (T - T_\infty) \quad (14)$$

where h_b is the convective heat transfer coefficient at the side and bottom surfaces of the workpiece which is $500.0 \text{ W}/(\text{m}^2 \text{ K})$ [48] in this study.

The slip rate (δ), used to determine the contact state between tool and workpiece, can be defined as [49],

$$\delta = \frac{\omega_M}{\omega_T} \quad (15)$$

where ω_M and ω_T are the angular velocity of the material adjacent to the tool and that of the tool, respectively.

The heat generation rate at shoulder-workpiece contact interface, pin bottom-workpiece interface and pin side-workpiece interface (only thread crest region for threaded pin) can be given as follows,

$$q(r) = [\delta \cdot \tau_y + (1 - \delta) \cdot \tau_f] \cdot \omega r \quad (16)$$

It is quite obvious that for the thread groove region at pin side surface, heat generation would be higher than that of the thread crest region of pin due to increase in contact area between pin and

workpiece. Thereby, the heat generation rate for the interface of workpiece-thread groove region of pin can be written as,

$$q(r) = \kappa [\delta \cdot \tau_y + (1 - \delta) \cdot \tau_f] \cdot \omega r \quad (17)$$

where κ is a constant used to account for an increase in contact area. Features such as thread on the pin are believed to increase heat generation rate due to the larger interfacial area [8]. For the pin profile used in this model, the total interfacial area in thread groove is about twice as much as that for the unthreaded pin. Therefore, the value of κ is taken as 2.0 in this work.

Due to a significant gap in thermal conductivities of tool and workpiece materials, only a part of the total heat generation at tool-workpiece interface could be transferred to the workpiece, equals to

$$q = \frac{J_W}{J_W + J_T} q(r) \quad (18)$$

where J_W and J_T are the total amount of heat conducted to the workpiece and tool, respectively,

$$J = \sqrt{k \rho c_p} \quad (19)$$

2.4. Velocity boundary conditions

In this model, the computation region is considered as a single-phase viscoplastic non-Newtonian fluid, and FSW tool is assumed to be rotating in a fixed position. As shown in Fig. 1, the material flows into the computation domain from the velocity-inlet and out from the velocity-outlet at the welding speed (corresponding to movement of worktable during welding). Bottom, top and side surfaces of the workpiece are considered equivalent to the wall surfaces, having same velocities as welding speed, but opposite in direction.

The velocity boundary conditions of the material adjacent to the tool at shoulder-workpiece contact interface, pin bottom-workpiece interface and pin side-workpiece interface (thread crest region for threaded pin) can be given as follows,

$$\begin{aligned} \vec{v}_x &= \delta \cdot \omega \cdot \vec{r} \cdot \sin \theta \\ \vec{v}_y &= \delta \cdot \omega \cdot \vec{r} \cdot \cos \theta \\ \vec{v}_z &= 0 \end{aligned} \quad (20)$$

For the thread groove region of pin side surface, the material velocity at the contact interface will be affected due to the presence of thread. Therefore, it is vital to analyze the effect of threads on flow characteristics of the material during welding.

3. Formulation of pin thread effect on material flow

3.1. Driving effect of thread on workpiece material adjacent to the pin

Due to the influence of driving force produced by pin thread, a large percentage of material adjacent to the pin will move downward when FSW tool with right-hand threaded pin rotates in a counter-clockwise direction, and the material near the TMAZ (thermo-mechanically affected zone) in shear layer will flow upwards [27]. Therefore, it is vital to take into account the driving force of pin thread quantitatively to analyze material flow across thread groove region.

In this study, the pin used has right-hand single-start thread with a rectangular cross-sectional shape, as shown in Fig. 2. The pitch is 1.0 mm, and the thread groove width is 0.5 mm. During FSW, the threaded pin is enveloped by the plastic material in shear layer, so that the threaded pin and the plastic material can be regarded as a screw thread pair consisting of the bolt with high strength (tool pin) and the nut with soft material (workpiece). As the tool rotates, the screw thread pair fails due to the plastic deformation of the softer workpiece material. Therefore, the characteristics of the material flow driven by the pin thread can be obtained by analyzing the interaction force between the

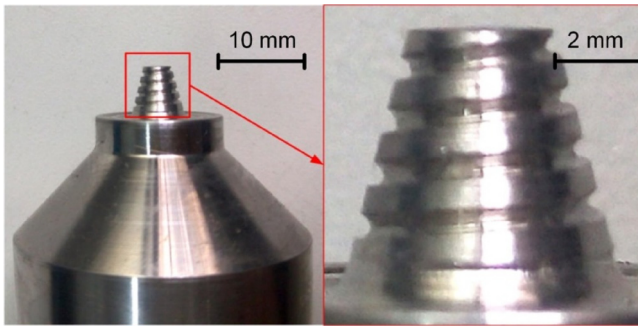


Fig. 2. Tool with threaded pin profile used in experimentation.

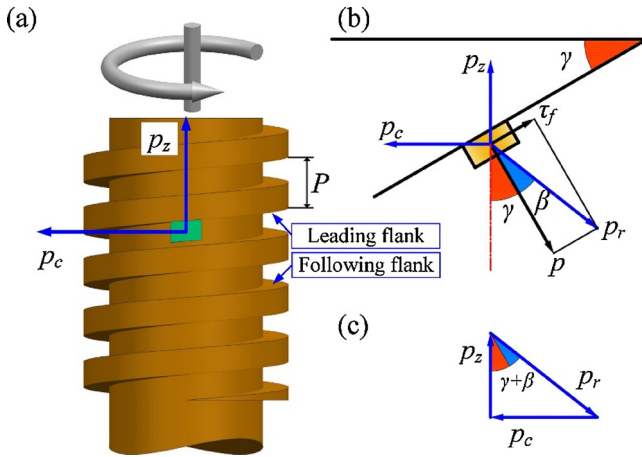


Fig. 3. Stress analysis between tool and workpiece when the tool rotates in counter-clockwise. (a) Schematic of thread in 3D, (b) interaction force between thread surface and workpiece material, (c) force triangle.

threaded pin and the workpiece material adjacent to the pin surface.

When the tool rotates in a counter-clockwise direction inside the workpiece material, the leading flank of the thread is responsible to drive the material flow [13]. As demonstrated in Fig. 3 (a), an elementary volume of plastic material in the thread groove can be treated as a sliding block which moves along the leading flank of the thread. If the leading flank of the thread is expanded, a slope with the angle of γ can be obtained. For sake of analysis, an elementary volume of plastic material can be taken out from the thread groove, and could be represented as analogues to a sliding block on an inclined plane as shown in Fig. 3 (b). The relative movement between the tool and the workpiece material can be considered as equivalent to the relative motion between the sliding block and the inclined plane. When the tool rotates, the counterforces exerted by the leading flank of the thread on the material come from two directions, i.e., the normal stress p along the normal direction of the leading flank of the thread and the tangent stress τ_f along the tangential direction of the leading flank of the thread. The resultant force of p and τ_f can be denoted as p_r , and the angle between p and p_r is defined as the friction angle β . Driven by the resultant force p_r , the material inside the thread groove will flow in counter-clockwise and downward direction meanwhile.

It should be noted that not only the leading flank of the thread applies a force on the workpiece material, but in turn, the latter also poses a reaction force on the former. This counterforce (acted on the leading flank of the thread by the workpiece material) can also be divided into two components, p_z in $+z$ direction and p_c in the peripheral direction. Under quasi-steady state welding condition, these three forces (p_z , p_c and p_r) can form a force triangle as depicted in Fig. 3 (c).

The friction angle β can be written as,

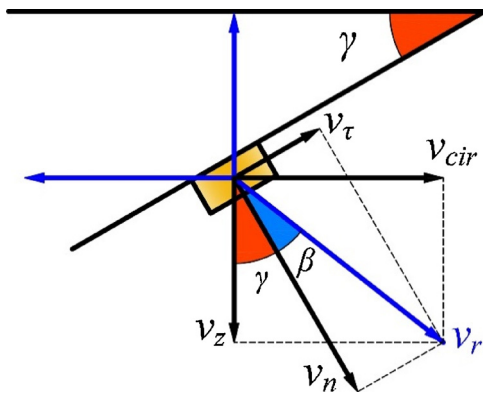


Fig. 4. Schematic illustration of the velocity boundary conditions caused by thread.

$$\beta = \arctan\left(\frac{\tau_f}{p}\right) \quad (21)$$

The lead angle γ shown in Fig. 3 (b) can be written as,

$$\gamma = \arctan\left(\frac{l}{2\pi r}\right) \quad (22)$$

where l is the lead of the helix, which is equal to the pitch (P) here, and r is the distance away from the tool axis.

As demonstrated in Fig. 4, the normal stress p and the tangent stress τ_f cause the material to flow along the normal direction of the leading flank of the thread and along the tangential direction of leading flank of the thread, respectively, which result in two components (v_n and v_t) of workpiece material flow. The workpiece material velocity (v_r) adjacent to the thread surface is in the direction of resultant force p_r . When the tool rotates, the tangential and axial components of material flow velocity (v_{cir} , v_z) can be determined as below,

$$v_{cir} = v_r \cdot \sin(\gamma + \beta) \quad (23)$$

$$v_z = v_r \cdot \cos(\gamma + \beta) \quad (24)$$

When tool rotates, the leading flank of thread associated with the tool also undergoes rotary motion. Based on the theory of thread cutting on the lathe, the value of velocity component in axial direction should satisfy following relation [50],

$$v_z = \frac{P\omega_p}{2\pi} \quad (25)$$

where ω_p is the relative angular velocity between the tool and that of the material adjacent to the tool.

Combining Eqs. (23)–(25), we can get,

$$v_r \cdot \cos(\gamma + \beta) = \frac{P}{2\pi} \left[\omega - \frac{v_r \cdot \sin(\gamma + \beta)}{r} \right] \quad (26)$$

After further manipulation, the resultant material velocity adjacent to the tool can be obtained by the following equation,

$$v_r = \frac{P\omega}{2\pi \cdot \cos(\gamma + \beta) + P \cdot \sin(\gamma + \beta)/r} \quad (27)$$

For the thread groove region, the workpiece material velocity adjacent to the tool comes from two parts. The first part is due to the frictional drive of pin side surface, and the second part is due to the drive of the thread. As there is a reduction in diameter of pin side surface due to the presence of thread groove, the first part of material velocity here is considered as 0.9 times that for thread crest region according to the actual tool pin used. Therefore, the boundary conditions of the material velocity adjacent to the tool at pin side-workpiece interface (thread groove region) can be given as follow,

$$\vec{v}_{cir} = \vec{v}_r \cdot \sin(\gamma + \beta) = \frac{P\omega \vec{r}}{2\pi r \cdot \cos(\gamma + \beta) + P \cdot \sin(\gamma + \beta)} \cdot \sin(\gamma + \beta) \quad (28)$$

$$\begin{aligned} \vec{v}_x &= 0.9 \times \delta \cdot \omega \cdot \vec{r} \cdot \sin \theta + \vec{v}_{cir} \cdot \sin \theta \\ &= 0.9 \times \delta \cdot \omega \cdot \vec{r} \cdot \sin \theta + \frac{P\omega \vec{r}}{2\pi r \cdot \cos(\gamma + \beta) + P \cdot \sin(\gamma + \beta)} \cdot \sin(\gamma + \beta) \cdot \sin \theta \end{aligned} \quad (29)$$

$$\begin{aligned} \vec{v}_y &= 0.9 \times \delta \cdot \omega \cdot \vec{r} \cdot \cos \theta + \vec{v}_{cir} \cdot \cos \theta \\ &= 0.9 \times \delta \cdot \omega \cdot \vec{r} \cdot \cos \theta + \frac{P\omega \vec{r}}{2\pi r \cdot \cos(\gamma + \beta) + P \cdot \sin(\gamma + \beta)} \cdot \sin(\gamma + \beta) \cdot \cos \theta \end{aligned} \quad (30)$$

$$\vec{v}_z = \vec{v}_r \cdot \cos(\gamma + \beta) = \frac{P\omega \vec{r}}{2\pi r \cdot \cos(\gamma + \beta) + P \cdot \sin(\gamma + \beta)} \cdot \cos(\gamma + \beta) \quad (31)$$

where θ is the angle relative to x -direction, and the \vec{r} is the radius vector.

3.2. Partitioning of thread crest and thread groove regions

As aforementioned, in this model the thread features are not considered in geometric model directly. The mesh used in the simulation for unthreaded and threaded pin is same. Thereby, the pin side surface needs to be identified separately as thread crest and thread groove regions so that suitable boundary conditions are implemented. Fig. 5 shows the helices on the pin side surface that divides the pin side surface into two separate regions. On the pin side surface, thread consists of two helices with a constant value of pitch. The thread groove width can be determined by the distance between two helices in z -direction.

In this study, the pitch is 1.0 mm, and the thread groove width is 0.5 mm. A conical pin is used. Its length is 5.7 mm, and its root and top diameters are 6.0 mm and 3.5 mm, respectively. An expression of equations describing two helices is depicted in Table 1.

4. Results & discussion

4.1. Effect of thread on material flow in shear layer

Fig. 6 shows a comparison of the material flow behavior for unthreaded and threaded pin profiles at the transverse cross-section of the weldment. Fig. 6 (a) presents the velocity vector at the transverse cross-section of the weldment for threaded pin profile, while Fig. 6 (b) and (c) are the magnified part of the local regions at RS and AS respectively. The red zone in Fig. 6 represents the predicted TMAZ. Fig. 6 (d) presents the velocity vector at the transverse cross-section of the weldment for unthreaded pin profile. Due to the large velocity gradient of material flow along the normal direction of the tool-workpiece interface

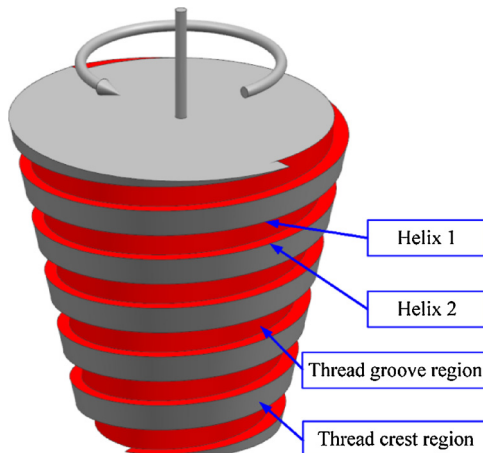


Fig. 5. The distinction of thread crest and thread groove regions on pin side surface.

Table 1
Equations of helices on pin side surface.

Helix 1	Helix 2
$m = 115/228 \cdot (1 - r/0.003)$	$m = 115/248 \cdot [1 - 19r/(62 \times 0.001)]$
$n = 6.2$	$n = 6.2$
$\theta_t = \left(m + \frac{\omega t}{2\pi \cdot n}\right) \cdot 360$	$\theta_t = \left(m + \frac{\omega t}{2\pi \cdot n}\right) \cdot 360$
$x_1 = r \cdot \cos(\theta_t \cdot n)$	$x_2 = r \cdot \cos(\theta_t \cdot n)$
$y_1 = -r \cdot \sin(\theta_t \cdot n)$	$y_2 = -r \cdot \sin(\theta_t \cdot n)$
$z_1 = -P \cdot n \cdot m + 0.006$	$z_2 = -P \cdot n \cdot m + 0.0065$

Note: m is a parameter having value from zero to one to determine the angle of helix rotating and the z -coordinate of the points on helices, r is the distance between a point on helix and tool axis, n is the helix winding number, θ_t is the angle of helix rotating when m increases from zero to one, (x_1, y_1, z_1) and (x_2, y_2, z_2) are the coordinates of the points on helices, t is the flow time.

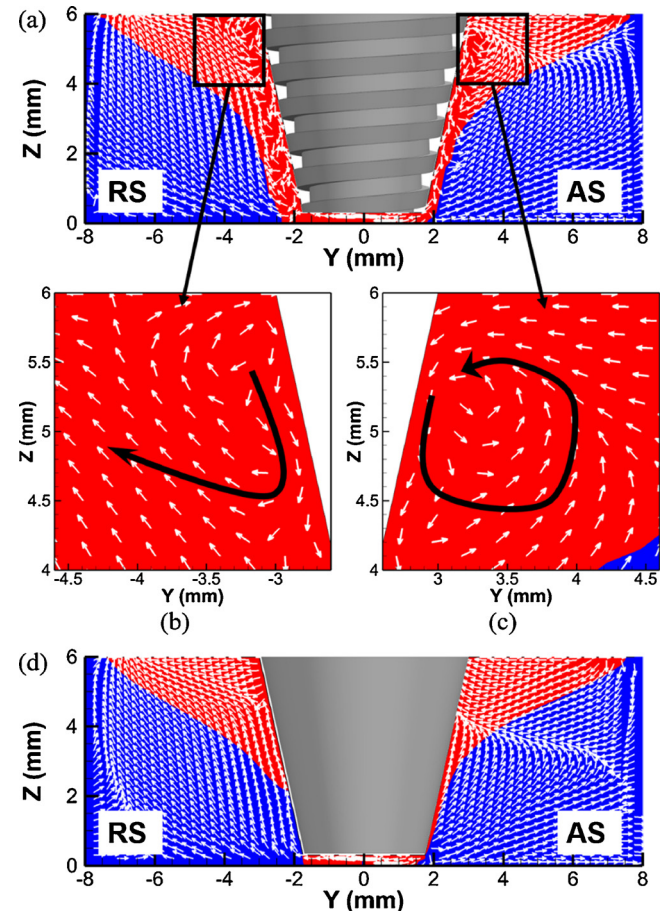


Fig. 6. The predicted material flow field at the transverse cross-section of the weld. (a) Velocity vector for a threaded pin, (b) enlarged local area at RS, (c) enlarged local area at AS, (d) velocity vector for an unthreaded pin.

during FSW, most vector size will be very small. It is difficult to show the movement trend of the material at the traverse cross-section of the weld if the vector size is used to represent the velocity magnitude. Therefore, the vector plotted in Fig. 6 just shows the direction of the component of the velocity at the traverse-cross section of the weld, but does not present the velocity magnitude.

It is evident that for threaded pin, the material adjacent to the pin surface has a tendency to flow downward, as shown in Fig. 6 (a). However, same phenomenon is not observed for unthreaded pin in Fig. 6 (d). As illustrated in Fig. 6 (b) and (c), material flow is in clockwise direction at RS, while at AS it is in a counter-clockwise direction. For threaded pin profile, the material moves downward close to

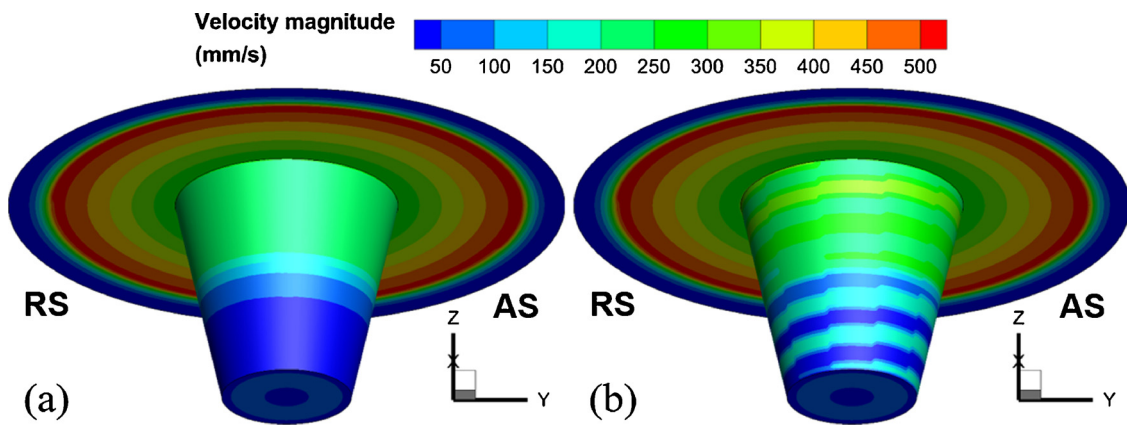


Fig. 7. Distribution of material flow velocity profile at tool-workpiece interface. (a) For unthreaded pin, (b) For threaded pin.

the pin side surface and reflows back when it reaches the bottom surface of the workpiece. Consequently, it flows upward near the border of shear layer, which enhances the mixing of material.

Fig. 7 shows the material flow velocity profile at the tool-workpiece interface for unthreaded and threaded pin, respectively. It is clear that at shoulder and pin bottom interface little difference in velocity distribution exists because of less effect of pin thread there. But at pin side surface, the material flow velocity profile is different for two cases. Especially at the lower part of pin side surface (nearer to the tip of the pin), the velocity at the area covered by pin thread is higher than that uncovered by pin thread, as shown in Fig. 7(b). For better understanding of the effect of pin thread on material flow in shear layer, detailed information analysis are carried out next.

At the horizontal plane $z = 3$ mm, a line along y -direction is selected. The line has two end points with the coordinates $(0, -3, 3)$ and $(0, 3, 3)$, as demonstrated in Fig. 8 (a). The distribution of material flow velocity along this line is drawn. Fig. 8 (b) compares the predicted average value of material flow velocity along this line for unthreaded

and threaded pin profiles. It is evident that the average flow velocity near the pin side surface is higher for threaded pin than that for unthreaded pin. As the distance away from the pin increases, the velocity difference gradually decreases for two cases. Beyond a certain point near the border of shear layer, the average material flow velocity for unthreaded pin becomes higher than that for threaded pin. It is affected by upward backflow caused by downward material flow close to the threaded pin side surface. Fig. 8 (c) shows the z -component of material flow velocity along the line. Near pin side surface in shear layer, the downward z -component of material flow velocity for threaded pin is obviously much higher than that for unthreaded pin. But as the distance away from the tool increases, the effect of thread on the velocity along z -direction becomes weaker and weaker. It is clear that the thread effect on material flow is only within a limited region near the pin, and the thread promotes the material transition along the vertical direction in shear layer.

As shown in Fig. 9 (a), two lines near and parallel to the pin side are selected at AS and RS to demonstrate the distribution of the average

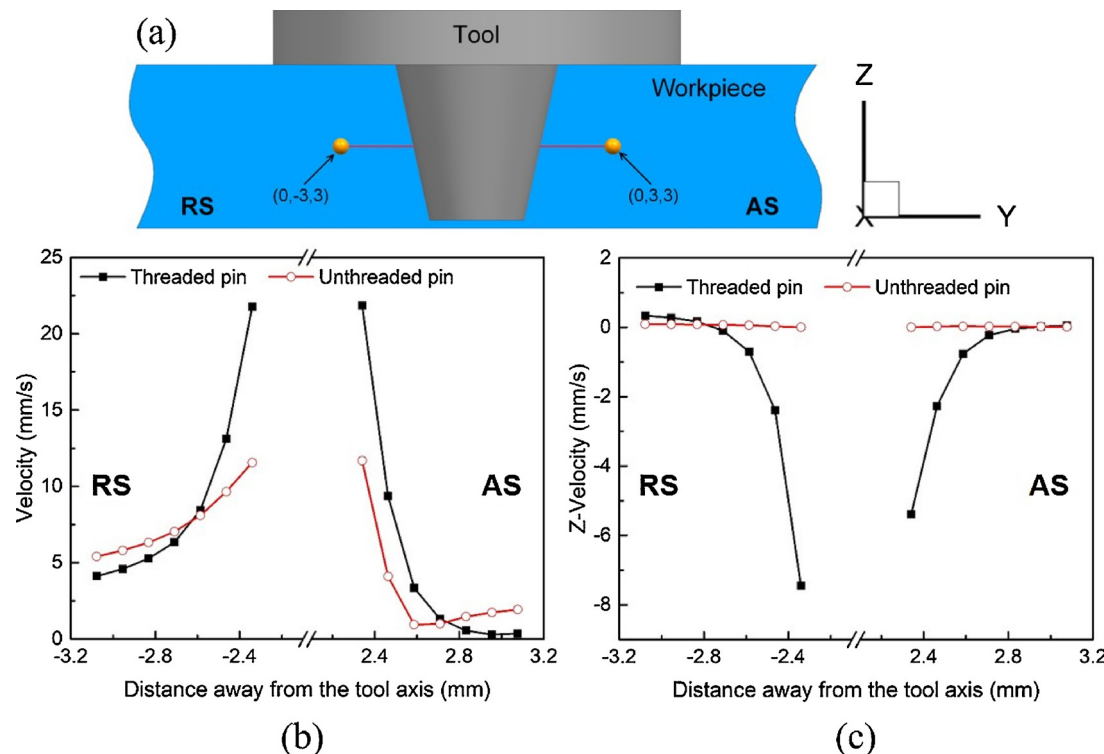


Fig. 8. The predicted material flow velocity along a line ($z = 3$ mm). (a) The line selected, (b) average velocity magnitude, (c) z -component of average velocity.

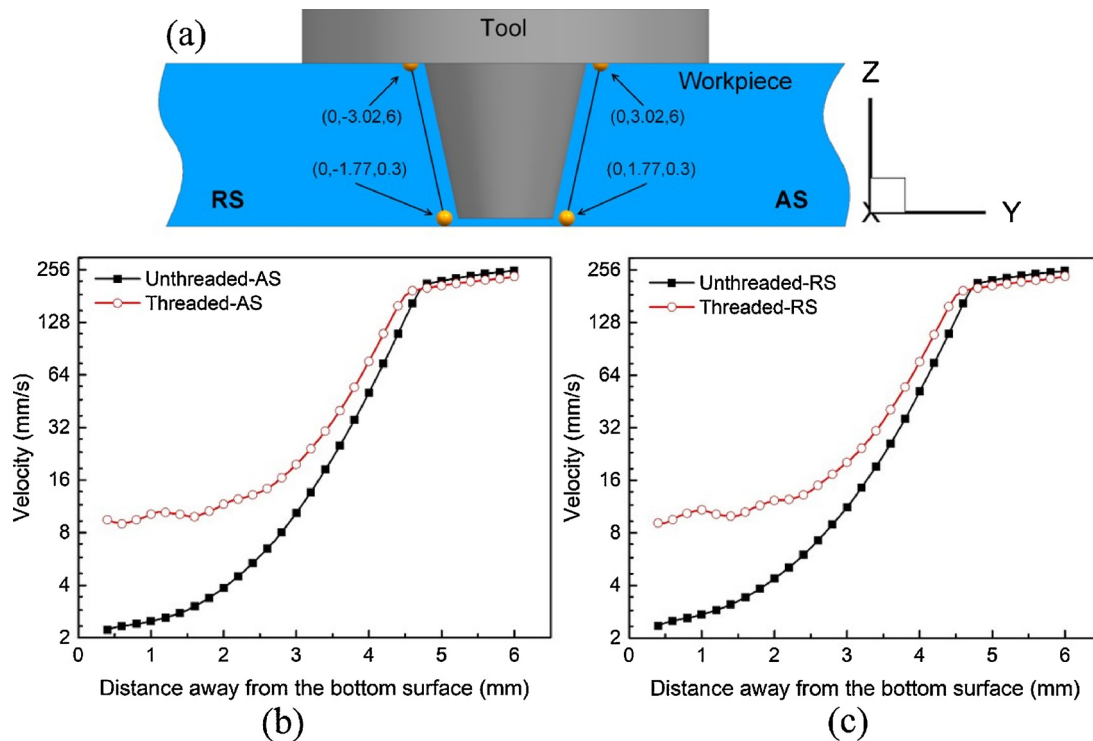


Fig. 9. The calculated average velocity of material flow for threaded and unthreaded pins. (a) The line selected, (b) AS, (c) RS.

velocity of material flow. Fig. 9 (b) and (c) illustrates a comparison of average velocity variation along these lines in shear layer for unthreaded and threaded pins. At AS, the magnitude of average velocity for threaded pin is larger than that for unthreaded pin, and this difference is quite notable close to the pin tip. It can be attributed to the forced driving effect of the thread on the material inside thread groove. On the other hand, the difference in average velocity decreases gradually as it approaches the pin root, because the effect of pin thread weakens near the shoulder region. The average velocity at RS shows a similar trend, as shown in Fig. 9 (c).

Fig. 10 (a) and (b) show the streamlines flow across unthreaded and threaded pins during FSW process for the plane 1 mm below tool shoulder surface. It can be observed that with threaded pin profile, the workpiece material is easily pushed into the stirring zone. The stirring zone is the region adjacent to the pin side in the shear layer and consisted of the rotation flow [18]. It is clear that the material flow is more intense for threaded pin compared to unthreaded one. The red dashed circle as shown in Fig. 10 (a) and (b) represent the region where the plastic material in front of the tool at AS flows in a counterclockwise

direction and passes by the tool at the RS. It is evident that material flow zone is quite enlarged for the threaded pin at a distance 1 mm below tool shoulder surface. It further emphasizes the occurrence of enhanced material flow for a threaded pin. For unthreaded pin, the diameter of the red dashed circle is 11 mm, but this value is 12 mm for threaded pin. This means that commonly occurring welding defects caused by inadequate material mixing across the weldment can be minimized or eliminated by using threaded pin profile. A similar observation of reduction on weldment defects for the threaded pin is also claimed by Reza-E-Rabby et al. [15]. As shown in Fig. 11 (a) and (b), streamlines at the plane 3 mm below tool shoulder surface shows a similar trend. However, the deformation zone at the plane 3 mm below tool shoulder surface becomes smaller than that at the horizontal plane 1 mm below tool shoulder surface, because the effect of shoulder weakens.

4.2. Effect of thread on heat generation and temperature distribution

Fig. 12 shows a comparison of calculated heat flux at the tool-

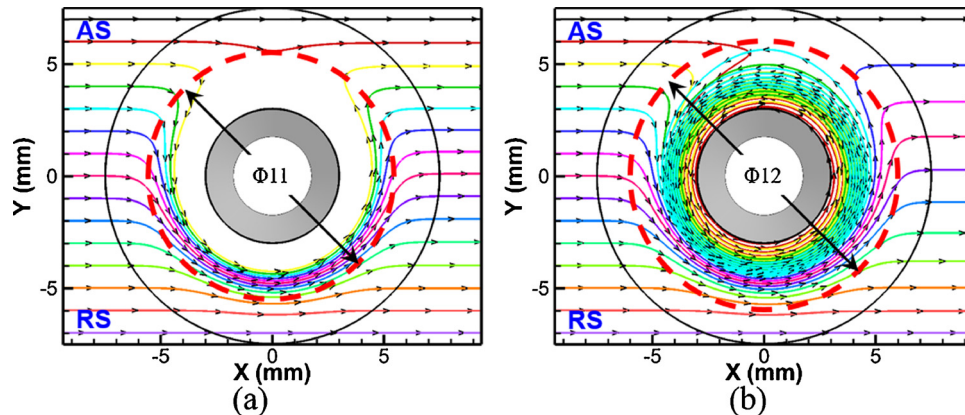


Fig. 10. Calculated streamlines near the tool at a distance of 1 mm below shoulder surface. (a) Unthreaded pin, (b) threaded pin.

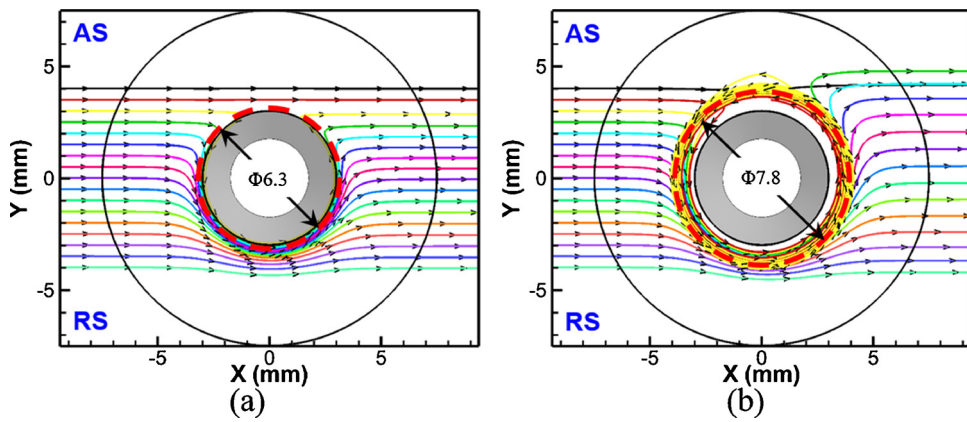


Fig. 11. Calculated streamlines near the tool at a distance of 3 mm below shoulder surface. (a) Unthreaded pin, (b) threaded pin.

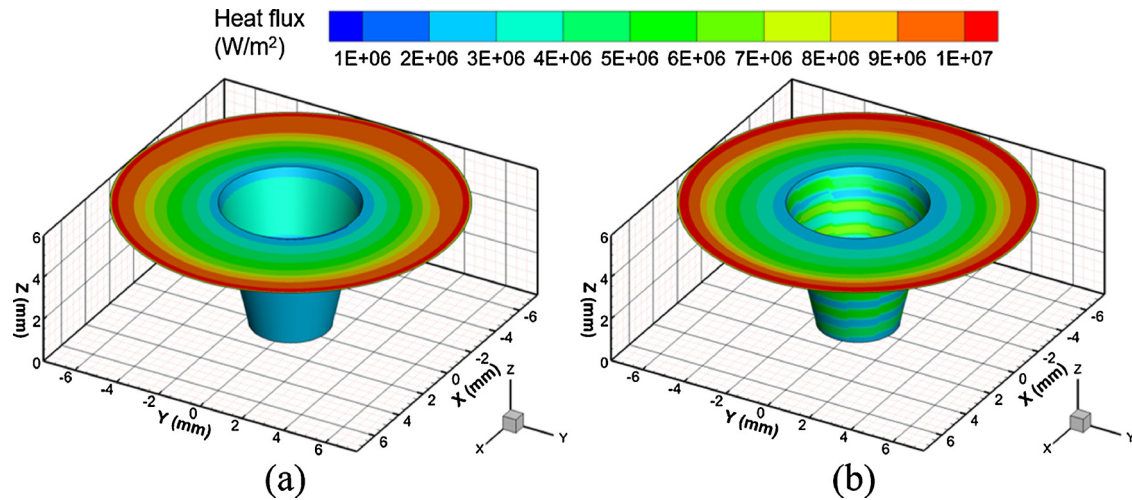


Fig. 12. Calculated heat flux at tool-workpiece interface.(a) Unthreaded pin, (b) threaded pin.

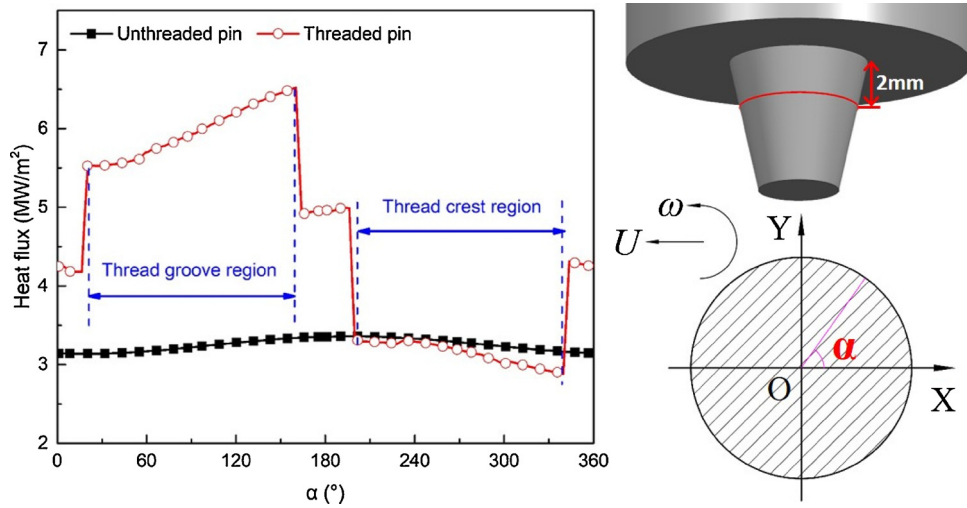


Fig. 13. Variation of calculated heat flux at pin side surface (2 mm below shoulder surface).

workpiece interface for unthreaded and threaded pins. It can be observed that magnitude of heat flux increases as the distance away from the tool axis gets larger, while its maxima occurs adjacent to edge of the tool shoulder owing to the large relative velocity between tool and material. Near the edge of shoulder, the difference of heat flux for unthreaded and threaded pins is quite less, because it is far from the pin side and there is almost no thread effect. At pin side-workpiece

interface, the distribution of the heat flux shows periodic fluctuation for threaded pin due to an increase in effective threaded contact area.

A circle on pin side is selected at a distance of 2 mm below shoulder surface. Fig. 13 shows a comparison of heat flux variation for unthreaded and threaded pin with respect to angle α along this circle. The heat flux at thread groove region of threaded pin is much higher than that of unthreaded pin. However, there is quite less difference between

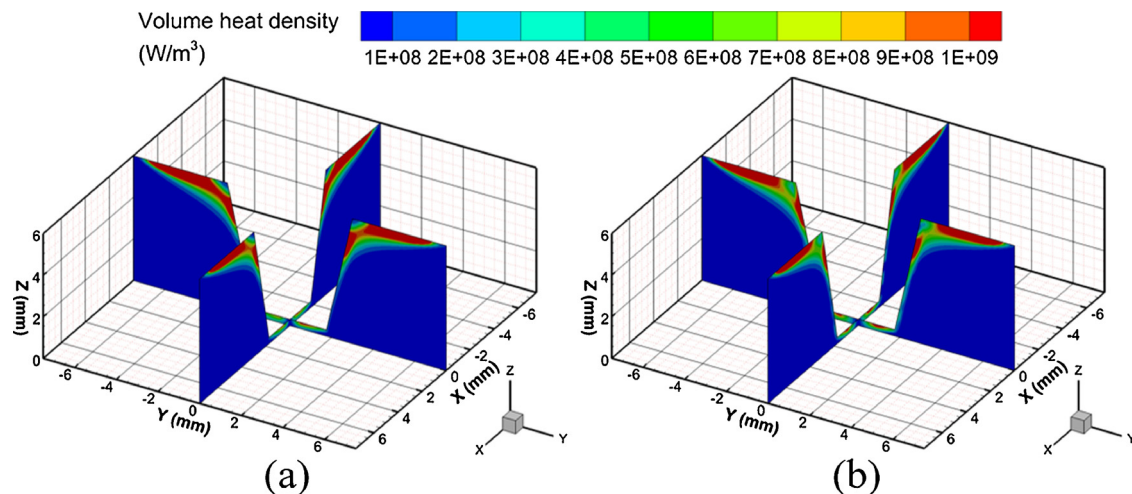


Fig. 14. Computed volumetric heat density in the shear layer. (a) Unthreaded pin; (b) threaded pin.

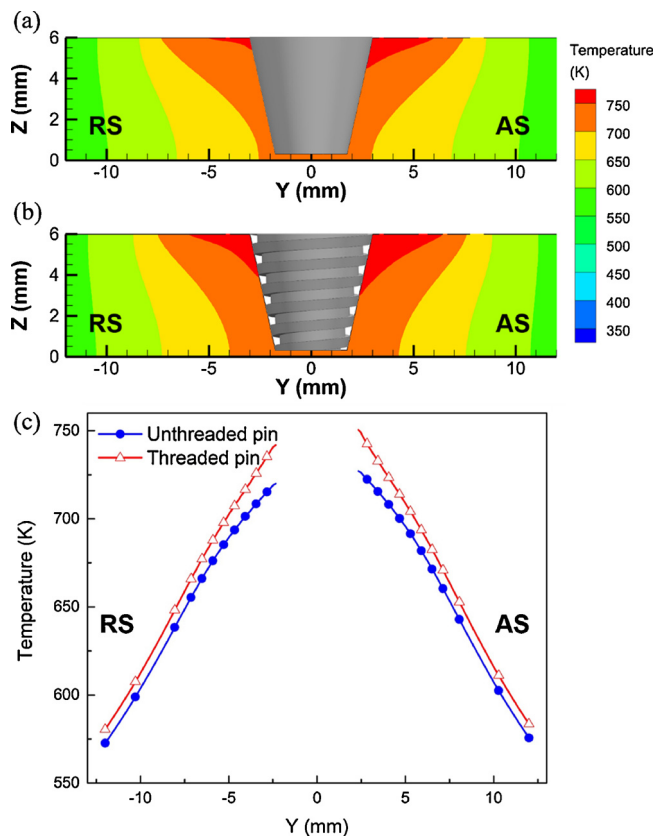


Fig. 15. Predicted temperature profile at transverse cross-section of the weldment. (a) Unthreaded pin, (b) threaded pin, (c) temperature distribution at plane $z = 3$ mm.

the heat flux at the thread crest region of threaded pin and that for unthreaded pin.

Fig. 14 (a) and (b) show the volumetric heat density due to viscous dissipation in the shear layer for unthreaded and threaded pin, respectively. It is evident that the distribution trend of volumetric heat density is quite similar for both the cases. For the sake of ease comparison, the shear layer zone can be divided into two regions, upper region ($z \geq 4$ mm) defined as Ω_1 , and the lower region ($z < 4$ mm) defined as Ω_2 . After integrating the volumetric heat density in Ω_1 and Ω_2 , the total heat generated for unthreaded pin comes out 152.5 W and 3.5 W in Ω_1 and Ω_2 , while that for the threaded pin is 142.0 W and

6.7 W. It is evident that pin thread has a great role in increasing the volumetric heat generation in Ω_2 which is near the bottom surface of the workpiece. This means that more heat generated near the threaded pin tip to soften the material and consequently improved material flow.

Fig. 15 shows the calculated temperature distribution at transverse cross-section for unthreaded and threaded pins. Referring to Fig. 15 (a) and (b), it is evident that the higher temperature region at upper half part (near shoulder) for threaded pin is larger than that for unthreaded pin. At the plane with half depth ($z = 3$ mm), the temperature variations with distance away from weldline for the unthreaded and threaded pins are plotted in Fig. 15 (c). It is clear that the temperature for threaded pin is slightly higher than that for unthreaded pin, because of an increase in contact interface area at the pin due to the presence of pin thread, which assists in additional heat generation into the weldment.

To validate the developed model, FSW experimentations were carried out using AA6061-T6 plates of 6 mm in thickness, 200 mm in length and 75 mm in width. Two such plates were in butt configuration. The tool shoulder diameter was 15 mm, and the diameter of the tapered pin was 3.5 mm at the tip and 6 mm at the root. The pin length was 5.7 mm. The tool rotation speed was 800 rpm, and welding speed was 150 mm/min. The tool tilt angle was kept at 2.5°, and shoulder plunge depth was 0.1 mm. K type thermocouples were embedded at a distance 10, 15 and 20 mm away from the weld centerline at AS and at a depth of 3 mm from the top surface of the workpiece. Fig. 16 (a) shows a comparison of calculated and measured temperature profiles at the point 15 mm away from the weld centerline for threaded pin, where the maximum value of predicted temperature profile is 551.4 K and that of measured one is 552.1 K, respectively. And 16 (b) shows the predicted and measured peak temperature values at three measurement points for unthreaded and threaded pin, respectively. It can be found that both are in good agreement with each other.

4.3. Effect of thread on TMAZ

The model is further experimentally verified by measuring the area of TMAZ in FSW. The test conditions were the same as aforementioned. For metallographic observation, after welding the specimen were cut perpendicular to the welding direction using wire EDM machine. The transverse cross-sections of the specimens were carefully grinded and polished and thereafter etched with 10% HF solutions. Low-magnification microscope was employed to obtain the macrostructure of the weldment.

The calculated TMAZ boundaries (show in red color) for unthreaded and threaded pin profiles are presented in Fig. 17 (a) and (b). TMAZ

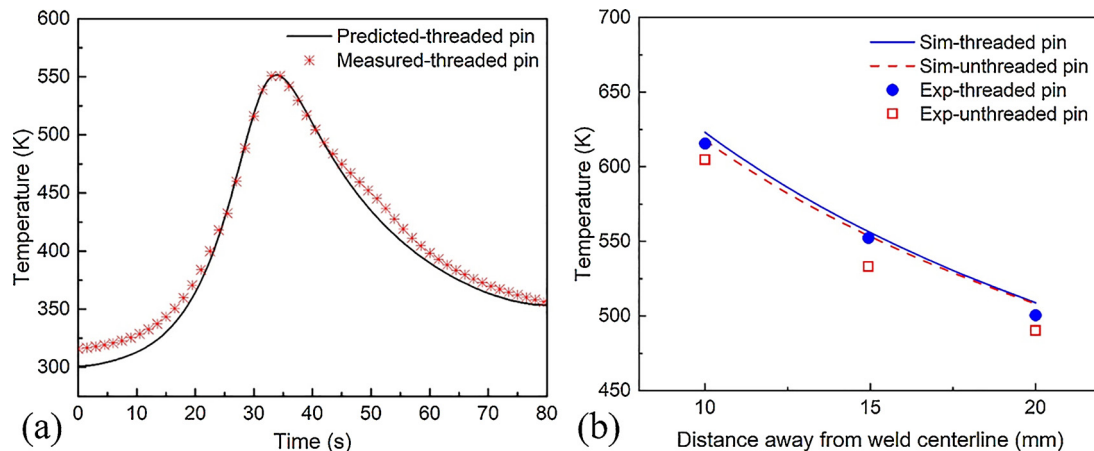


Fig. 16. Comparison of measured and predicted temperature.(a) Temperature profile for threaded pin, (b) peak temperature at different points at AS for unthreaded and threaded pin.

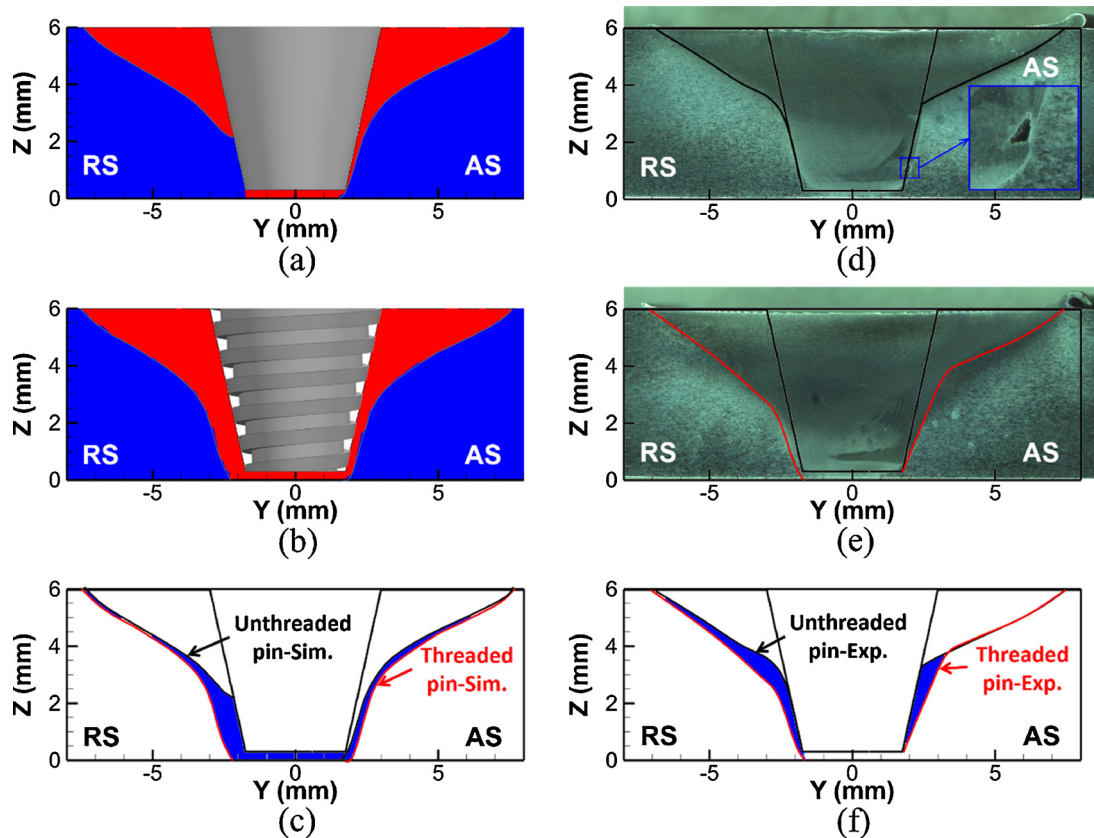


Fig. 17. The TMAZ boundary for unthreaded and threaded pins.

(a) The predicted TMAZ for unthreaded pin, (b) the predicted TMAZ for threaded pin, (c) comparison of calculated TMAZ, (d) the measured TMAZ for unthreaded pin, (e) the measured TMAZ for threaded pin, (f) comparison of measured TMAZ.

Table 2
Predicted and measured area of TMAZ (mm^2).

	Unthreaded pin	Threaded pin	Increment
Computed	168.5	183.56	15.1
Measured	152.2	168.4	16.2

boundary is defined as the zone whose viscosity is lower than 5×10^6 Pa·s [51]. Fig. 17 (c) compares the predicted TMAZ boundaries for unthreaded and threaded pin profiles. The area covered by TMAZ boundaries for threaded pin is larger than that for unthreaded pin.

Especially, the width of TMAZ adjacent to pin tip is increased by thread. As shown in Fig. 17 (a), the predicted width of TMAZ near the pin tip is almost the same as the pin diameter. In such a case, little plastic deformation takes place there, and the material there is difficult to flow. Consequently, it leads to the formation of weld defects more easily. Therefore, the threaded pin is expected to promote the material flow close to the bottom surface of the workpiece, which is beneficial to minimizing or eliminating of weld defects there. Fig. 17 (b) and (d) present the experimentally measured TMAZ under same welding parameters for unthreaded and threaded pins. A comparison of measured TMAZ boundaries for unthreaded and threaded pin profiles is

shown in Fig. 17 (f). It is clear that threaded pin increases the area of TMAZ because it enhances plastic material flow around the pin.

Table 2 gives the predicted and measured area of TMAZ. The predicted area of TMAZ for threaded pin is 183.56 mm², which is about 15.1 mm² larger than that for an unthreaded pin. The experimental results show that the measured area of TMAZ for the threaded pin is 168.4 mm², which is 16.2 mm² larger than that for an unthreaded pin. It is clear the thread pin results in an increase in the area of TMAZ by 10.6%. In addition, the numerically simulated TMAZ area is in agreement with the experimentally measured one.

5. Conclusions

- (1) The interaction force between the thread groove and the workpiece material is analyzed, and special equations are derived to describe the effect of pin thread parameters on the material flow velocity inside thread grooves. These equations are combined with a three-dimensional transient CFD model to quantitatively analyze the effect of threaded pin profile on heat generation, temperature field and material flow in FSW.
- (2) The results show that when tool rotates in counter-clockwise direction, a right-hand threaded pin can push the material near the pin side to flow downward, which causes an upward motion of an equivalent amount of material near the border of the shear layer. Near pin side surface in shear layer, the downward z-component of material flow velocity for threaded pin is much higher than that for unthreaded pin.
- (3) The average flow velocity near the pin side surface is higher for threaded pin than that for unthreaded pin. As the distance away from the pin increases, the velocity difference for two pins gradually decreases.
- (4) Near pin side, pin thread results in a little bit increase in heat generation because thread makes the area of pin/workpiece contact interface enlarged. For a threaded pin, the area of TMAZ is broadened, especially the width of TMAZ near the bottom surface of the workpiece, and the material is easily pushed into the stirring zone. The pin thread is proven to effectively improve the material flow near the pin tip.
- (5) The experiments were conducted to validate the method and model. The calculated and measured thermal cycles and TMAZ boundary match with each other. Compared with the sliding mesh method, this model is easier to ensure the numerical robustness and save computational time.

Acknowledgement

The authors acknowledge the financial support from the National Natural Science Foundation of China (Grant No. 51475272).

References

- [1] Padhy GK, Wu CS, Gao S. Friction stir based welding and processing technologies - processes, parameters, microstructures and applications: a review. *J Mater Sci Technol* 2018;34(1):1–38.
- [2] Liu FC, Hovanski Y, Miles MP, Sorensen CD, Nelson TW. A review of friction stir welding of steels: tool, material flow, microstructure, and properties. *J Mater Sci Technol* 2018;34(1):39–57.
- [3] Çam G, Mistikoglu S. Recent developments in friction stir welding of Al-alloys. *J Mater Eng Perform* 2014;23(6):1936–53.
- [4] Mishra RS, Ma ZY. Friction stir welding and processing. *Mater Sci Eng R Rep* 2005;50(1–2):1–78.
- [5] Banik A, Roy BS, Barma JD, Saha SC. An experimental investigation of torque and force generation for varying tool tilt angles and their effects on microstructure and mechanical properties: friction stir welding of AA 6061-T6. *J Manuf Process* 2018;31:395–404.
- [6] Zhao YH, Lin SB, Wu L, Qu FX. The influence of pin geometry on bonding and mechanical properties in friction stir weld 2014 Al alloy. *Mater Lett* 2005;59(23):2948–52.
- [7] Hajideh MR, Farahani M, Alavi SAD, Ramezani NM. Investigation on the effects of tool geometry on the microstructure and the mechanical properties of dissimilar friction stir welded polyethylene and polypropylene sheets. *J Manuf Process* 2017;26:269–79.
- [8] Rai R, De A, HKDH Bhadeshia, DebRoy T. Review: friction stir welding tools. *Sci Technol Weld Joining* 2013;16(4):325–42.
- [9] Mugada KK, Adepu K. Influence of ridges shoulder with polygonal pins on material flow and friction stir weld characteristics of 6082 aluminum alloy. *J Manuf Process* 2018;32:625–34.
- [10] Huang Y, Xie Y, Meng X, Lv Z, Cao J. Numerical design of high depth-to-width ratio friction stir welding. *J Mater Process Technol* 2018;252:233–41.
- [11] Nandan R, DebRoy T, Bhadeshia H. Recent advances in friction-stir welding—process, weldment structure and properties. *Prog Mater Sci* 2008;53(6):980–1023.
- [12] Elangovan K, Balasubramanian V. Influences of tool pin profile and tool shoulder diameter on the formation of friction stir processing zone in AA6061 aluminium alloy. *Mater Des* 2008;29(2):362–73.
- [13] Chowdhury SM, Chen DL, Bhole SD, Cao X. Tensile properties of a friction stir welded magnesium alloy: effect of pin tool thread orientation and weld pitch. *Mater Sci Eng A* 2010;527(21):6064–75.
- [14] Zhang YN, Cao X, Larose S, Wanjarla P. Review of tools for friction stir welding and processing. *Can Metall Quart* 2013;51(3):250–61.
- [15] Reza-E-Rabbi M, Tang W, Reynolds AP. Effects of thread interruptions on tool pins in friction stir welding of AA6061. *Sci Technol Weld Joining* 2017;23(2):114–24.
- [16] Zettler R, Lomolino S, Dos Santos JF, Donath T, Beckmann F, Lippman T, et al. A study on material flow in FSW of AA 2024-T351 and AA 6056-T4 alloys. 5th International FSW Symposium-Metz France. 2004.
- [17] Ouyang J, Kovacevic R. Material flow and microstructure in the friction stir butt welds of the same and dissimilar aluminum alloys. *J Mater Eng Perform* 2002;11(1):51–63.
- [18] Schmidt HNB, Dickerson TL, Hattel JH. Material flow in butt friction stir welds in AA2024-T3. *Acta Mater* 2006;54(4):1199–209.
- [19] Morisada Y, Fujii H, Kawahito Y, Nakata K, Tanaka M. Three-dimensional visualization of material flow during friction stir welding by two pairs of X-ray transmission systems. *Scripta Mater* 2011;65(12):1085–8.
- [20] Morisada Y, Imaizumi T, Fujii H. Determination of strain rate in friction stir welding by three-dimensional visualization of material flow using X-ray radiography. *Scripta Mater* 2015;106:57–60.
- [21] Colegrove PA, Shercliff HR. Experimental and numerical analysis of aluminium alloy 7075-T7351 friction stir welds. *Sci Technol Weld Joining* 2003;8(5):360–8.
- [22] Nandan R, Roy G, Liener T, Debroy T. Three-dimensional heat and material flow during friction stir welding of mild steel. *Acta Mater* 2007;55(3):883–95.
- [23] Shi L, Wu CS, Liu HJ. Modeling the material flow and heat transfer in reverse dual-rotation friction stir welding. *J Mater Eng Perform* 2014;23(8):2918–29.
- [24] Schmidt H, Hattel J. A local model for the thermomechanical conditions in friction stir welding. *Modell Simul Mater Sci Eng* 2005;13(1):77–93.
- [25] Zhang Z. Comparison of two contact models in the simulation of friction stir welding process. *J Mater Sci* 2008;43(17):5867–77.
- [26] Colegrove PA, Shercliff HR. Development of Trivex friction stir welding tool Part 2 - three-dimensional flow modelling. *Sci Technol Weld Joining* 2004;9(4):352–61.
- [27] Ji SD, Shi QY, Zhang LG, Zou AL, Gao SS, Zan LV. Numerical simulation of material flow behavior of friction stir welding influenced by rotational tool geometry. *Comput Mater Sci* 2012;63:218–26.
- [28] Chen GQ, Shi QY, Fujii Y, Horie T. Simulation of metal flow during friction stir welding based on the model of interactive force between tool and material. *J Mater Eng Perform* 2014;23(4):1321–8.
- [29] Su H, Wu CS, Bachmann M, Rethmeier M. Numerical modeling for the effect of pin profiles on thermal and material flow characteristics in friction stir welding. *Mater Des* 2015;77:114–25.
- [30] Liechty BC, Webb BW. Modeling the frictional boundary condition in friction stir welding. *Int J Mach Tools Manuf* 2008;48(12–13):1474–85.
- [31] Chen G, Feng Z, Zhu Y, Shi Q. An alternative frictional boundary condition for computational fluid dynamics simulation of friction stir welding. *J Mater Eng Perform* 2016;25(9):4016–23.
- [32] Su H, Wu CS, Pittner A, Rethmeier M. Thermal energy generation and distribution in friction stir welding of aluminum alloys. *Energy* 2014;77:720–31.
- [33] Shi L, Wu CS, Liu XC. Modeling the effects of ultrasonic vibration on friction stir welding. *J Mater Process Technol* 2015;222:91–102.
- [34] Jain R, Pal SK, Singh SB. A study on the variation of forces and temperature in a friction stir welding process: a finite element approach. *J Manuf Process* 2016;23:278–86.
- [35] Schmidt H, Hattel J. Modelling heat flow around tool probe in friction stir welding. *Sci. Technol. Weld Joining* 2013;10(2):176–86.
- [36] Nandan R, Roy G, Debroy T. Improving reliability of heat transfer and material flow calculations during friction stir welding of dissimilar aluminum alloys. *Weld J* 2007;86(10):313–22.
- [37] Shi L, Wu CS, Padhy GK, Gao S. Numerical simulation of ultrasonic field and its acoustoplastic influence on friction stir welding. *Mater Des* 2016;104:102–15.
- [38] Yang CL, Wu CS, Lv XQ. Numerical analysis of mass transfer and material mixing in friction stir welding of aluminum/magnesium alloys. *J Manuf Process* 2018;32:380–94.
- [39] Colegrove PA, Shercliff HR. 3-Dimensional CFD modelling of flow round a threaded friction stir welding tool profile. *J Mater Process Technol* 2005;169(2):320–7.
- [40] Yu Z, Zhang W, Choo H, Feng Z. Transient heat and material flow modeling of friction stir processing of magnesium alloy using threaded tool. *Metall Mater Trans A* 2011;43(2):724–37.
- [41] Atharifar H, Lin D, Kovacevic R. Numerical and experimental investigations on the loads carried by the tool during friction stir welding. *J Mater Eng Perform* 2008;18(4):339–50.

- [42] Chen G, Li H, Wang G, Guo Z, Zhang S, Dai Q, et al. Effects of pin thread on the in-process material flow behavior during friction stir welding: a computational fluid dynamics study. *Int J Mach Tools Manuf* 2018;124:12–21.
- [43] Arora A, De A, DebRoy T. Toward optimum friction stir welding tool shoulder diameter. *Scripta Mater* 2011;64(1):9–12.
- [44] Zienkiewicz OC, Cormeau IC. Visco-plasticity - plasticity and creep in elastic solids - a unified numerical solution approach. *Int J Numer Methods Eng* 1974;8(4):821–45.
- [45] Sun Z, Wu CS, Kumar S. Determination of heat generation by correlating the interfacial friction stress with temperature in friction stir welding. *J Manuf Process* 2018;31:801–11.
- [46] Sheppard T, Jackson A. Constitutive equations for use in prediction of flow stress during extrusion of aluminium alloys. *Mater Sci Technol* 1997;13(3):203–9.
- [47] Wen CD, Mudawar I. Modeling the effects of surface roughness on the emissivity of aluminum alloys. *Int J Heat Mass Transf - Theory Appl* 2006;49(23–24):4279–89.
- [48] Yu M, Li WY, Li JL. Modelling of entire friction stir welding process by explicit finite element method. *Mater Sci Technol* 2012;28(7):812–7.
- [49] Schmidt H, Hattel J, Wert J. An analytical model for the heat generation in friction stir welding. *Modell Simul Mater Sci Eng* 2004;12(1):143–57.
- [50] Youssef HA, El-Hofy HA. *Machining technology: machine tools and operations*. CRC Press; 2008.
- [51] Nandan R, Roy G, Debroy T. Numerical simulation of three-dimensional heat transfer and plastic flow during friction stir welding. *Metall Mater Trans A* 2006;37(4):1247–59.